University of Thessaly
School of Engineering
Department of Mechanical Engineering

Master Thesis

THREE DIMENSIONAL UNIT CELL MODELING OF MULTIPHASE STEELS

by

ANASTASIOS GIOMPLIAKIS

A Thesis
Submitted in Partial Fulfilment of the
Requirements for the Degree of
Master of Science
2014

The approval of the Master Thesis by the Department of Mechanical Engineering, School of Engineering, University of Thessaly does not imply acceptance of the author's views (N. 5343/32 $\alpha\rho$. 202 $\pi\alpha\rho$. 2).

Approved by the Three Members of the Advisory Committee:

First Member   *Nikolaos Aravas*
(Supervisor)   *Professor of Computational Mechanics,*
Department of Mechanical Engineering, University of Thessaly

Second Member   *Gregory Haidemenopoulos*
Professor of Physical Mettalurgy,
Department of Mechanical Engineering, University of Thessaly

Third Member   *Alexis Kermanidis*
Assistant Professor of Mechanical Behavior of Metallic Materials,
Department of Mechanical Engineering, University of Thessaly

Acknowledgments

This thesis was carried out at the Laboratory of Mechanics & Strength of Materials under the Master of Science Program of the Department of Mechanical Engineering of University of Thessaly (UTH).

I would like to thank my supervisor, Professor Nikolaos Aravas for everything that I learned working next to him, his patience and valuable assistance, whenever I have needed it. Our cooperation has been a strong motive and privilege for me.

I would also like to thank all my friends and fellow students for their help, moral support and the wonderful moments that we shared during all these years.

Last but not least, I thank my family for making it possible for me to attend and complete my Master Studies and for all the invaluable things they have offered me.

Abstract

The technological progress on every level of engineering, has increased the demand of materials that combine a wide variety of mechanical properties. The most promising answer to this demand has been the evolution of composite materials. One of the most important aspects of which, are the multiphase steels. In the following thesis, we deal with the prediction of the overall properties, of such a multiphase steel, given the properties of its individual phases, as well as their volume fractions.

To start with, a homogenization theory is presented for the approach of the properties of a given composite. Then, the described procedure is incorporated into a UMAT subroutine, in order to be numerically tested through the simulation of a uniaxial tension test, in ABAQUS general purpose finite element program.

Following that, we would like to check the consistency of the homogenization theory, as well as create a variety of unit cells, that can be considered a representative part of the microstructure of a composite. To do so, we create 2D axisymmetric and 3D cubic unit cells and test them against the Homogenization technique. The main focus of this thesis, is on the modeling of 3D unit cells, which are, as we will see, considered a far more realistic model of an actual composite.

Subsequently, we analyze a more simple case of a composite, that of a dual phase steel, and compare the results of all the methods described in the following pages, for various volume fractions of the inclusion phase. Finally, we introduce a more complex, three-phase cubic unit cell, which can be considered more representative of an actual TRIP steel, and compare it to the homogenization technique.

Contents

List of Figures

Chapter 1

Homogenization Theory

1.1 Introduction

In this chapter, we would like to determine the corresponding constitutive equation for a composite material, made up of N phases. The total deformation rate is written as the sum of the elastic and plastic parts.

$$\mathbf{D} = \mathbf{D}^e + \mathbf{D}^p \tag{1.1}$$

In the following, we discuss in detail the constitutive equations for the individual parts of $\mathbf{D}$, and the homogenization technique used to derive them.

1.2 Elastic constitutive relations

The elastic properties of each of the N phases are essentially the same and the composite material is assumed to be homogeneous in the elastic region. Standard isotropic linear hypoelasticity is assumed and the constitutive equation for $\mathbf{D}^e$ is written as:

$$\mathbf{D}^e = \boldsymbol{\mathcal{M}}^e : \overset{\triangledown}{\boldsymbol{\sigma}} \qquad \text{or} \qquad \overset{\triangledown}{\boldsymbol{\sigma}} = \boldsymbol{\mathcal{L}}^e : \mathbf{D}^e, \tag{1.2}$$

where $\overset{\triangledown}{\boldsymbol{\sigma}}$ is the Jaumann derivative of the stress tensor $\boldsymbol{\sigma}$, $\boldsymbol{\mathcal{M}}^e$ is the elastic compliance tensor defined as

$$\boldsymbol{\mathcal{M}}^e = \frac{1}{2\,\mu}\,\mathbf{K} + \frac{1}{3\,\kappa}\,\mathbf{J}, \qquad \boldsymbol{\mathcal{L}}^e = \boldsymbol{\mathcal{M}}^{e-1} = 2\,\mu\,\mathbf{K} + 3\,\kappa\,\mathbf{J}, \qquad \mathbf{J} = \frac{1}{3}\,\boldsymbol{\delta}\,\boldsymbol{\delta}, \qquad \mathbf{K} = \mathbf{I} - \mathbf{J}, \tag{1.3}$$

μ and κ denote the elastic shear and bulk moduli, $\boldsymbol{\delta}$ and $\mathbf{I}$ the second- and symmetric fourth-order identity tensors, with Cartesian components δ_{ij} (the Kronecker delta) and $I_{ijkl} = (\delta_{ik}\,\delta_{jl} + \delta_{il}\,\delta_{jk})/2$.

1.3 Constitutive equations for $\mathbf{D}^p$

The plastic deformation rate, is given in the form:

$$\mathbf{D}^p = \dot{\bar{\varepsilon}}^p \mathbf{N} \qquad \text{with} \qquad \dot{\bar{\varepsilon}}^p = \dot{\varepsilon}_0 \left[\frac{\sigma_{eq}}{\sigma_y\left(\bar{\varepsilon}^p\right)} \right]^m \qquad \text{and} \qquad \mathbf{N} = \frac{3}{2}\,\frac{\mathbf{s}}{\sigma_{eq}} \tag{1.4}$$

where $\dot{\varepsilon}_0$ is a reference value for the strain rate, m is the strain-rate-sensitivity exponent of the material, $\sigma_{eq} = \sqrt{\frac{3}{2}\mathbf{s} : \mathbf{s}}$ is the von Mises equivalent stress, $\mathbf{s}$ is the deviatoric stress tensor, and $\sigma_y\left(\bar{\varepsilon}^p\right)$ is the yield stress of the material at the reference strain rate $\dot{\varepsilon}_0$.

The hardening behavior of each individual phase, is described as a function of equivalent plastic strain ε^p according to equation (1.5).

$$\sigma_y\left(\bar{\varepsilon}^p\right) = \sigma_0\left(1 + \frac{\bar{\varepsilon}^p}{\varepsilon_0}\right)^{1/n} \tag{1.5}$$

where σ_0, ε_0 are reference values for yield stress and strain respectively with $\sigma_0 = E\varepsilon_0$ (E the Young modulus), n is the hardening exponent, and $\bar{\varepsilon}^p = \int_0^t \dot{\bar{\varepsilon}}^p dt$ is the equivalent plastic strain.

Each phase is assumed to be plastically incompressible and the corresponding constitutive equations are written in terms of a "viscous potentials" of the "power-law" type $U^{(r)} = U^{(r)}\left(\sigma_{eq}\right)$.

1.4 Homogenization technique

We consider an isotropic composite, consisting of N incompressible viscous phases distributed uniformly and isotropically with dissipation functions of the "power-law" type:

$$U^{(r)}\left(\sigma\right) = \frac{1}{n^{(r)}+1}\sigma_0^{(r)}\dot{\varepsilon}_0^{(r)}\left(\frac{\sigma_{eq}}{\sigma_0^{(r)}}\right)^{n^{(r)}+1}, \qquad \text{where} \qquad \sigma_{eq} = \sqrt{\frac{3}{2}\mathbf{s} : \mathbf{s}}, \qquad \mathbf{s} = \sigma - \frac{\sigma_{kk}}{3}\delta,$$

so that

$$\mathbf{D} = \frac{\partial U^{(r)}}{\partial \sigma} = \dot{\bar{\varepsilon}}\,\mathbf{N} = \frac{\mathbf{s}}{2\,\mu^{(r)}\left(\mathbf{s}\right)}, \qquad \dot{\bar{\varepsilon}} = \sqrt{\frac{2}{3}\mathbf{D} : \mathbf{D}} = \dot{\varepsilon}_0^{(r)}\left(\frac{\sigma_{eq}}{\sigma_0^{(r)}}\right)^{n^{(r)}}, \qquad \mathbf{N} = \frac{3}{2\,\sigma_{eq}}\mathbf{s},$$

$$\mu^{(r)}\left(\sigma_{eq}\right) = \frac{1}{3}\frac{\sigma_0^{(r)}}{\dot{\varepsilon}_0^{(r)}}\left(\frac{\sigma_0^{(r)}}{\sigma_{eq}}\right)^{n^{(r)}-1}.$$

There are two interesting limiting cases of the above described model.

- For $n^{(r)} = 1$ (Linear material)

$$U_L^{(r)} = \frac{1}{2}\sigma_0^{(r)}\dot{\varepsilon}_0^{(r)}\left(\frac{\sigma_{eq}}{\sigma_0^{(r)}}\right)^2 = \frac{\sigma_{eq}^2}{6\mu^{(r)}} \tag{1.6}$$

Where

$$\mu^{(r)} = \frac{\sigma_0^{(r)}}{3\dot{\varepsilon}_0^{(r)}}, \qquad \text{and} \qquad \dot{\bar{\varepsilon}}^{p(r)} = \frac{\sigma_{eq}}{3\mu^{(r)}} = \dot{\varepsilon}_0^{(r)}\frac{\sigma_{eq}}{\sigma_0^{(r)}}$$

- For $n^{(r)} \to \infty$ (Rigid-Perfectly-Plastic material)

Taking into account that $\lim\limits_{n \to \infty} \frac{A^{n+1}}{n+1} = \begin{cases} 0 & if \quad A \leq 1, \\ \infty & if \quad A > 1, \end{cases}$ we conclude that:

$$U^{(r)} = \lim_{n^{(r)} \to \infty} \left[\frac{1}{n^{(r)}+1} \sigma_0^{(r)} \dot{\varepsilon}_0^{(r)} \left(\frac{\sigma_{eq}}{\sigma_0^{(r)}} \right)^{n^{(r)}+1} \right] = \begin{cases} 0 & if \quad \frac{\sigma_{eq}}{\sigma_0^{(r)}} \leq 1 \\ \infty & if \quad \frac{\sigma_{eq}}{\sigma_0^{(r)}} > 1 \end{cases} \tag{1.7}$$

The dissipation function of the composite is defined by (Ponte [10] eqns (3.6) & (3.2), Ponte [11] eqns (5.18) & (5.19), Ponte [12] eq (4.52))

$$\tilde{U}\left(\bar{\sigma}\right) = \sup_{\mu^{(r)} \geq 0} \left\{ \tilde{U}_L\left(\bar{\sigma}_{eq}, \tilde{\mu}\left(\mu^{(r)}\right)\right) - \sup_{\sigma_{eq}^{(r)} \geq 0} \sum_{r=1}^{N} c^{(r)} \left[U_L^{(r)}\left(\sigma_{eq}^{(r)}, \mu^{(r)}\right) - U^{(r)}\left(\sigma_{eq}^{(r)}\right) \right] \right\} \tag{1.8}$$

where

$$\tilde{U}_L = \frac{\bar{\sigma}_{eq}^2}{6\,\tilde{\mu}\left(\mu^{(r)}\right)}, \qquad U_L^{(r)} = \frac{\left(\sigma_{eq}^{(r)}\right)^2}{6\,\mu^{(r)}}. \tag{1.9}$$

The corresponding constitutive equation for the composite is

$$\bar{\mathbf{D}} = \frac{\partial \tilde{U}}{\partial \bar{\sigma}}.$$

Where $\bar{\mathbf{D}}$ and $\bar{\sigma}$ are the macroscopic deformation rate and stress tensors respectively.

Optimization of (1.8) w.r.t. $\sigma_{eq}^{(r)}$:

$$\frac{\partial \tilde{U}}{\partial \sigma_{eq}^{(r)}} = \frac{\partial}{\partial \sigma_{eq}^{(r)}} \left\{ \sum_{s=1}^{N} c^{(s)} \left[U_L^{(s)}\left(\sigma_{eq}^{(s)}, \mu^{(s)}\right) - U^{(s)}\left(\sigma_{eq}^{(s)}\right) \right] \right\} = c^{(r)} \left(\frac{\sigma_{eq}^{(r)}}{3\,\mu^{(r)}} - \frac{\partial U^{(r)}}{\partial \sigma_{eq}^{(r)}} \right) =$$

$$= c^{(r)} \left[\frac{\sigma_{eq}^{(r)}}{3\,\mu^{(r)}} - \dot{\varepsilon}_0^{(r)} \left(\frac{\sigma_{eq}^{(r)}}{\sigma_0^{(r)}} \right)^{n^{(r)}} \right] = 0 \quad \Rightarrow \quad \sigma_{eq}^{(r)} = \left[\frac{\left(\sigma_0^{(r)}\right)^{n^{(r)}}}{3\,\mu^{(r)}\,\dot{\varepsilon}_0^{(r)}} \right]^{\frac{1}{n^{(r)}-1}} \equiv \hat{\sigma}_{eq}^{(r)}$$

Substituting $\sigma_{eq}^{(r)} = \hat{\sigma}_{eq}^{(r)}$ in (1.8), we find

$$\tilde{U} = \sup_{\mu^{(r)} \geq 0} \left[\frac{\bar{\sigma}_{eq}^2}{6\,\tilde{\mu}\left(\mu^{(r)}\right)} - \frac{1}{2} \sum_{r=1}^{N} \frac{n^{(r)}-1}{n^{(r)}+1} \left(\frac{\left(\sigma_0^{(r)}\right)^{n^{(r)}}}{\dot{\varepsilon}_0^{(r)}} \right)^{\frac{2}{n^{(r)}-1}} \frac{c^{(r)}}{\left(3\,\mu^{(r)}\right)^{\frac{n^{(r)}+1}{n^{(r)}-1}}} \right] \tag{1.10}$$

The effective modulus $\tilde{\mu}$ for particulate composites is estimated as

$$\tilde{\mu}\left(\mu^{(r)}\right) = \frac{\displaystyle\sum_{s=1}^{N} \frac{c^{(s)}\,\mu^{(s)}}{3\,\mu_0+2\,\mu^{(s)}}}{\displaystyle\sum_{r=1}^{N} \frac{c^{(r)}}{3\,\mu_0+2\,\mu^{(r)}}} \qquad \text{or} \qquad \frac{\mu^{(1)}}{\tilde{\mu}} = \frac{\displaystyle\sum_{r=1}^{N} \frac{c^{(r)}\,y^{(r)}}{3\,\frac{y^{(r)}}{y_0}+2}}{\displaystyle\sum_{s=1}^{N} \frac{c^{(s)}}{3\,\frac{y^{(s)}}{y_0}+2}} \equiv \frac{T_1\left(y^{(i)}\right)}{T_2\left(y^{(i)}\right)} \equiv F\left(y^{(i)}\right)$$

where $\qquad y^{(r)} = \frac{\mu^{(1)}}{\mu^{(r)}}\ \left(y^{(1)}=1\right) \qquad$ and $\qquad y_0 = \frac{\mu^{(1)}}{\mu_0} = y_0\left(y^{(r)}\right).$

Examples:

i)For $\qquad \mu_0 = \mu^{(1)}, \qquad$ we have that $\qquad y_0 = 1 \qquad \Rightarrow \qquad \frac{\partial y_0}{\partial y^{(r)}} = 0.$

ii)For $\qquad \mu_0 = \sum_{r=1}^{N} c^{(r)}\,\mu^{(r)} \qquad$ (Voigt model), $\qquad \frac{1}{y_0} = \frac{\mu_0}{\mu^{(1)}} = \sum_{r=1}^{N} c^{(r)}\,\frac{\mu^{(r)}}{\mu^{(1)}} = \sum_{r=1}^{N} \frac{c^{(r)}}{y^{(r)}}$

$\Rightarrow \qquad \frac{1}{y_0^2}\frac{\partial y_0}{\partial y^{(i)}} = -\frac{c^{(i)}}{y^{(i)2}} \qquad \Rightarrow \qquad \frac{\partial y_0}{\partial y^{(i)}} = c^{(i)}\left(\frac{y_0}{y^{(i)}}\right)^2$

iii)For $\qquad \frac{1}{\mu_0} = \sum_{r=1}^{N} \frac{c^{(r)}}{\mu^{(r)}} \qquad$ (Reuss model), $\qquad y_0 = \frac{\mu^{(1)}}{\mu_0} = \sum_{r=1}^{N} c^{(r)}\,\frac{\mu^{(1)}}{\mu^{(r)}} = \sum_{r=1}^{N} c^{(r)}\,y^{(r)}$

$\Rightarrow \qquad \frac{\partial y_0}{\partial y^{(i)}} = y^{(i)}$

iv)Self-consistent scheme $\qquad \mu_0 = \frac{\displaystyle\sum_{s=1}^{N} \frac{c^{(s)}\,\mu^{(s)}}{3\,\mu_0+2\,\mu^{(s)}}}{\displaystyle\sum_{r=1}^{N} \frac{c^{(r)}}{3\,\mu_0+2\,\mu^{(r)}}} \qquad \Rightarrow \qquad \frac{1}{\mu_0} = \frac{\displaystyle\sum_{r=1}^{N} \frac{c^{(r)}}{3\,\mu_0+2\,\mu^{(r)}}}{\displaystyle\sum_{s=1}^{N} \frac{c^{(s)}\,\mu^{(s)}}{3\,\mu_0+2\,\mu^{(s)}}}$

$\Rightarrow \qquad \frac{\mu^{(1)}}{\mu_0} = \frac{\displaystyle\sum_{r=1}^{N} \frac{c^{(r)}}{3\,\frac{\mu_0}{\mu^{(1)}}+2\,\frac{\mu^{(r)}}{\mu^{(1)}}}}{\displaystyle\sum_{s=1}^{N} \frac{c^{(s)}\,\frac{\mu^{(s)}}{\mu^{(1)}}}{3\,\frac{\mu_0}{\mu^{(1)}}+2\,\frac{\mu^{(s)}}{\mu^{(1)}}}} \qquad \Rightarrow \qquad y_0 = \frac{\displaystyle\sum_{r=1}^{N} \frac{c^{(r)}}{\frac{3}{y_0}+\frac{2}{y^{(r)}}}}{\displaystyle\sum_{s=1}^{N} \frac{\frac{c^{(s)}}{y^{(s)}}}{\frac{3}{y_0}+\frac{2}{y^{(s)}}}} \qquad \Rightarrow \qquad y_0 = \frac{\displaystyle\sum_{r=1}^{N} \frac{c^{(r)}\,y^{(r)}}{3\,\frac{y^{(r)}}{y_0}+2}}{\displaystyle\sum_{s=1}^{N} \frac{c^{(s)}}{3\,\frac{y^{(s)}}{y_0}+2}}$

Then equation (1.10) becomes:

$$\tilde{U} = \sup_{\substack{y^{(r)}\geq 0 \\ y^{(1)}=1}} \sup_{\mu^{(1)}>0} \left[F\left(y^{(r)}\right)\frac{\bar{\sigma}_{eq}^2}{6\,\mu^{(1)}} - I\left(\mu^{(1)},y^{(r)}\right)\right], \tag{1.11}$$

where

$$I\left(\mu^{(1)},y^{(r)}\right) = \frac{1}{2}\sum_{r=1}^{N} c^{(r)}\frac{n^{(r)}-1}{n^{(r)}+1}\left[\frac{\left(\sigma_0^{(r)}\right)^{n^{(r)}}}{\dot{\varepsilon}_0^{(r)}}\right]^{\frac{2}{n^{(r)}-1}}\left(\frac{y^{(r)}}{3\,\mu^{(1)}}\right)^{\frac{n^{(r)}+1}{n^{(r)}-1}} \tag{1.12}$$

Optimization of (1.11) with respect to $\mu^{(1)}$ and $y^{(r)}$, and taking into account that:

$$\frac{\partial \tilde{U}}{\partial \mu^{(1)}} = 0 \qquad \text{and} \qquad \frac{\partial \tilde{U}}{\partial y^{(r)}} = 0$$

leads into the optimal values:

$$\mu^{(1)} = \hat{\mu}^{(1)}\left(\bar{\sigma}_{eq}, c^{(s)}, \sigma_0^{(s)}\right) \qquad \text{and} \qquad y^{(r)} = \hat{y}^{(r)}\left(\bar{\sigma}_{eq}, c^{(s)}, \sigma_0^{(s)}\right).$$

The optimal value of $\tilde{U}$ is defined from (1.11):

$$\tilde{U}\left(\bar{\sigma}_{eq}\right) = \frac{1}{6}\frac{F\left(\hat{y}^{(r)}\left(\bar{\sigma}_{eq}\right)\right)}{\hat{\mu}^{(1)}\left(\bar{\sigma}_{eq}\right)}\,\bar{\sigma}_{eq}^2 - I\left(\hat{\mu}^{(1)}\left(\bar{\sigma}_{eq}\right), \hat{y}^{(r)}\left(\bar{\sigma}_{eq}\right)\right) \tag{1.13}$$

and the flow rule is:

$$\bar{\mathbf{D}} = \frac{\partial \tilde{U}}{\partial \bar{\sigma}} = \underbrace{\frac{\partial \tilde{U}}{\partial \bar{\sigma}_{eq}}}_{\equiv \dot{\bar{\varepsilon}}} \underbrace{\frac{\partial \bar{\sigma}_{eq}}{\partial \bar{\sigma}}}_{\mathbf{N}} \equiv \dot{\bar{\varepsilon}}\,\mathbf{N}, \qquad \mathbf{N} = \frac{\partial \bar{\sigma}_{eq}}{\partial \bar{\sigma}} = \frac{3}{2\,\bar{\sigma}_{eq}}\bar{\mathbf{s}}$$

Finally:

$$\bar{\mathbf{D}} = \dot{\bar{\varepsilon}}\,\mathbf{N} = \frac{\bar{\sigma}_{eq}}{3\,\tilde{\mu}}\,\mathbf{N} = \frac{\bar{\mathbf{s}}}{2\,\tilde{\mu}}, \qquad \tilde{\mu} = \tilde{\mu}\left(\hat{\mu}^{(r)}\right).$$

1.4.1 The case where all creep exponents are equal

In the case where $n^{(1)} = n^{(2)} = \cdots = n^{(N)} \equiv n$, the dissipation function of the composite given by equation (1.10) takes the form:

$$\tilde{U} = \sup_{\mu^{(r)} \geq 0}\left\{\frac{\bar{\sigma}_{eq}^2}{6\,\tilde{\mu}\left(\mu^{(r)}\right)} - \frac{n-1}{2\,(n+1)}\sum_{r=1}^{N}\frac{c^{(r)}}{\left(3\,\mu^{(r)}\right)^{\frac{n+1}{n-1}}}\left[\frac{\left(\sigma_0^{(r)}\right)^n}{\dot{\varepsilon}_0^{(r)}}\right]^{\frac{2}{n-1}}\right\},$$

which can be written also as:

$$\tilde{U} = \sup_{\substack{y^{(r)} \geq 0 \\ y^{(1)}=1}}\sup_{\mu^{(1)} > 0}\left[\frac{\bar{\sigma}_{eq}^2}{6\,\mu^{(1)}}F\left(y^{(r)}\right) - \frac{n-1}{2\,(n+1)}\frac{1}{\left(3\,\mu^{(1)}\right)^{\frac{n+1}{n-1}}}H\left(y^{(r)}\right)\right], \tag{1.14}$$

where now

$$F\left(y^{(r)}\right) = \frac{\mu^{(1)}}{\tilde{\mu}} = \frac{\displaystyle\sum_{r=1}^{N}\frac{c^{(r)}\,y^{(r)}}{3\frac{y^{(r)}}{y_0}+2}}{\displaystyle\sum_{s=1}^{N}\frac{c^{(s)}}{3\frac{y^{(s)}}{y_0}+2}} \qquad \text{and} \qquad H\left(y^{(r)}\right) = \sum_{r=1}^{N}c^{(r)}\left[\frac{\left(\sigma_0^{(r)}\right)^n}{\dot{\varepsilon}_0^{(r)}}\right]^{\frac{2}{n-1}}\left(y^{(r)}\right)^{\frac{n+1}{n-1}}.$$

Through the optimality conditions of the previous section, we subtitute the optimal values of $\mu^{(1)} = \hat{\mu}^{(1)}\left(y^{(r)}\right)$ and $\hat{y}^{(i)} = \hat{y}^{(i)}\left(c^{(r)}, \sigma_0^{(r)}\right)$ into equation (1.14), which reduces into:

$$\tilde{U} = \frac{\bar{\sigma}_{eq}^{n+1}}{n+1}\sqrt{\sup_{y^{(r)} \geq 0}\left\{\frac{\left[F\left(y^{(r)}\right)\right]^{n+1}}{\left[H\left(y^{(r)}\right)\right]^{n-1}}\right\}} = \frac{\bar{\sigma}_{eq}^{n+1}}{n+1}\sqrt{\frac{F(\hat{y}^{(r)})^{n+1}}{H(\hat{y}^{(r)})^{n-1}}}. \tag{1.15}$$

Remarks: The optimal values of $\hat{y}^{(i)} = \hat{y}^{(i)}\left(c^{(r)}, \sigma_0^{(r)}\right)$ are independent of $\bar{\sigma}_{eq}$, and the composite dissipation function is of the power-law type.

1.4.2 Perfect Plasticity

For the case where all creep exponents are equal and $n \to \infty$ (Perfect Plasticity), we can write the dissipation function in the form:

$$\tilde{U} = \frac{1}{n+1}\left\{\bar{\sigma}_{eq}^2 \sup_{\substack{y^{(r)} \geq 0 \\ y^{(1)} = 1}}\left[\frac{F\left(y^{(r)}\right)}{H(y^{(r)})^{\frac{n-1}{n+1}}}\right]\right\}^{\frac{n+1}{2}}. \tag{1.16}$$

Taking into account that $\qquad \lim_{x \to \infty}\left\{\left[\frac{a(x)}{x}\right]^{x/2}\right\} = \begin{cases} 0 & \text{when} \quad a\left(\infty\right) \leq 1, \\ \infty & \text{when} \quad a\left(\infty\right) > 1, \end{cases}$

we conclude

$$\lim_{n \to \infty}\tilde{U} = \begin{cases} 0 & \text{when} \quad \bar{\sigma}_{eq}^2 \sup_{\substack{y^{(r)} \geq 0 \\ y^{(1)} = 1}}\left[\frac{F\left(y^{(r)}\right)}{H^\infty\left(y^{(r)}\right)}\right] \leq 1, \\ \infty & \text{when} \quad \bar{\sigma}_{eq}^2 \sup_{\substack{y^{(r)} \geq 0 \\ y^{(1)} = 1}}\left[\frac{F\left(y^{(r)}\right)}{H^\infty\left(y^{(r)}\right)}\right] > 1, \end{cases} \tag{1.17}$$

where

$$F\left(y^{(r)}\right) = \frac{\mu^{(1)}}{\tilde{\mu}} = \frac{\sum\limits_{r=1}^{N}\frac{c^{(r)}\,y^{(r)}}{3\frac{y^{(r)}}{y_0}+2}}{\sum\limits_{s=1}^{N}\frac{c^{(s)}}{3\frac{y^{(s)}}{y_0}+2}}, \qquad H^\infty\left(y^{(r)}\right) = \lim_{n \to \infty}H\left(y^{(r)}\right) = \sum_{r=1}^{N}c^{(r)}\left(\sigma_0^{(r)}\right)^2 y^{(r)} \equiv \sigma_\infty^2\left(y^{(r)}\right). \tag{1.18}$$

Comparing equation (1.17) with equation (1.7) we conclude that the composite material obeys a von-Mises-like yield criterion with a flow stress $\bar{\sigma}_0$ defined by

$$\bar{\sigma}_0 = \sqrt{\inf_{\substack{y^{(r)} \geq 0 \\ y^{(1)} = 1}} \left[\frac{\sum\limits_{r=1}^{N} \frac{c^{(r)} y^{(r)}}{3 \frac{y^{(r)}}{y_0} + 2}}{\sum\limits_{s=1}^{N} \frac{c^{(s)}}{3 \frac{y^{(s)}}{y_0} + 2}} \left(\sum_{t=1}^{N} c^{(t)} \left(\sigma_0^{(t)} \right)^2 y^{(t)} \right) \right]} = \sqrt{\frac{\sigma_\infty^2 \left(\hat{y}^{(r)} \right)}{F \left(\hat{y}^{(r)} \right)}} \qquad (1.19)$$

1.5 Introduction of the UMAT subroutine

ABAQUS general purpose finite element program, provides a general interface so that a particular constitutive model can be introduced as a "user subroutine" (UMAT). This user subroutine will be called at all material calculation points of elements, for which the material definition includes a user-defined material behavior, and can be used with any procedure that includes mechanical behavior.

The use of a certain UMAT subroutine, requires a proper definition of the constitutive equation, that means explicit definition of stress (Cauchy stress for large-strain applications). Then the constitutive rate equation is transformed into an incremental equation using a suitable integration procedure:

- Forward Euler (explicit integration)

- Backward Euler (implicit integration)

- Midpoint method

It is essential to use a Backward Euler integration scheme, in order to be able to use increments of reasonable size and achieve a higher stability of the integration procedure.

The calculation of the Jacobian matrix is also required.

- For small-deformation problems the consistent Jacobian is:

$$\mathbf{C} = \frac{\partial \Delta \boldsymbol{\sigma}}{\partial \Delta \boldsymbol{\varepsilon}},$$

where $\Delta \boldsymbol{\sigma}$ is the increment in (Cauchy) Stress and $\Delta \boldsymbol{\varepsilon}$ is the increment in strain.

- If large deformations with large volume changes are considered (e.g., pressure-dependent plasticity), the exact form of the consistent Jacobian should be used to ensure rapid convergence:

$$\mathbf{C} = \frac{1}{J} \frac{\partial \Delta \left(J \boldsymbol{\sigma} \right)}{\partial \Delta \boldsymbol{\varepsilon}}$$

Here J is the determinant of the deformation gradient $\mathbf{F}$.

Eventually, the role of UMAT is to pass in all the information at the start of the increment, i.e., $\mathbf{F}_n$, $\boldsymbol{\sigma}_n$, $\bar{\varepsilon}_n^{p(r)}$ as well as $\mathbf{F}_{n+1}$, and the user has to calculate the values of the corresponding quantities at the end of the increment, i.e., $\boldsymbol{\sigma}_{n+1}$, and $\bar{\varepsilon}_{n+1}^{p(r)}$.

The homogenization technique described above, is imported into ABAQUS through the UMAT subroutine, and a single-element uniaxial tension test is carried out in order to check the validity of the homogenization theory. The results of the single-element test are then compared to a variety of unit cells that are examined in the next chapters and the final results can be seen in chapter 4.

Chapter 2

2D Unit cell

2.1 Introduction

In this Chapter we consider a two-phase TRIP steel made of an austenitic matrix that contains dispersed martensite. The reason that we choose these two phases, in order to compare the finite element calculations with the Homogenization technique, is that they offer the biggest difference between their yields. So one can say that we check the worst case scenario of a dual phase steel. The volume fractions of the two phases are assumed to remain constant as the composite deforms. The homogenization technique is used to determine the overall behavior of the two-phase steel.

In order to check the results of the homogenization technique in the best possible way, we create various unit cells, from a simple 2D axisymmetric unit cell to a more complex 3D unit cell that we can see in the next chapter (Chapter 3). Then, finite element calculations for the corresponding problem of uniaxial tension are carried out, for all of the various unit cells, and the results are compared with those of the homogenization theory, expressed through the UMAT subroutine.

The first kind of unit cell that we will look into is a simple 2D axisymmetric unit cell made of two phases. As we will conclude later, this kind of unit cell is considered very practical, since it requires minimum computer time in order to be meshed and processed. However it offers reliable results only for small volume fractions of the inclusion material ($c = 10 - 20\%$). In the following pages we see the whole process by which we can create such a unit cell and carry out various finite element simulations.

2.2 Modeling the microstructure of a two-phase metal

We assume that the two-phase composite that we examine, consists of particles of martensite isotropically and homogeneously dispersed in the austenitic matrix phase. The microstructure of the composite material can be described approximately by a three-dimensional periodic array of identical prismatic cells. Every cell models the two phases of the composite and consists of a martensitic spherical inclusion embedded in the center of a hexagonal prism,

simulating the austenitic matrix. Figure 2.1 shows a schematic representation of the three-dimensional periodic array of prismatic cells. The periodic array of prismatic cells shown in Figure 2.1 is extended in all three directions.
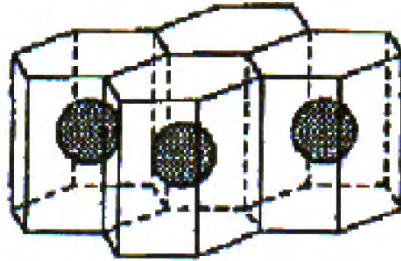

Figure 2.1: Three dimensional periodic array of prismatic cells.

In order to minimize the calculations, as well as make the problem an axisymmetric one, we replace the prismatic cells with the corresponding cylindrical cells as shown in Fig. 2.2 and 2.3. It is important to mention that, in order to minimize the errors generated by this approximation, we assume that the volume of the cylindrical cell is equal to that of the prismatic.

Figure 2.3 also depicts the appropriate dimensions of such a cylindrical cell. The spherical
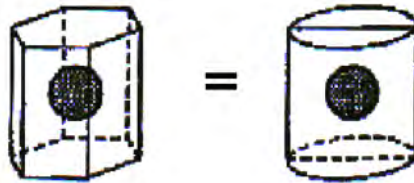

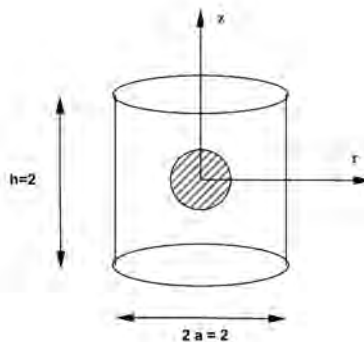Figure 2.2: A cylindrical approach to a prismatic unit cell.

Figure 2.3: Dimensions of the cylindrical unit cell.

inclusion embedded in the center of the cylinder models the martensitic particles as mentioned above, and its radius R is related with the volume fraction of martensite $c^{(2)}$ according

to equation (2.1):

$$c^{(2)} = \frac{V_{sphere}}{V_{total}} = \frac{\frac{4}{3}\pi R^3}{2\pi a^3} = \frac{2}{3}\left(\frac{R}{a}\right)^3 \qquad \Rightarrow \qquad \frac{R}{a} = \left(\frac{3\,c^{(2)}}{2}\right)^{1/3}, \tag{2.1}$$

where we have taken into account that the height h of the unit cell is equal to $2\,a$.

The axisymmetric problem is symmetric about the midplane $z = 0$, therefore we need to model only one quarter of the cross-section on the $z - r$ plane, as shown in Figure 2.4, where the dark area represents the martensitic phase.
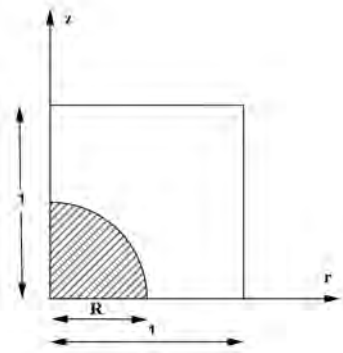

Figure 2.4: Final approximation of a prismatic unit cell.

A typical finite element mesh used in the calculations is shown in Fig. 2.5. The mesh consists of 870 4-node axisymmetric elements (CAX4H in ABAQUS). The blue elements correspond to the martensitic particles and the red are the austenitic matrix.
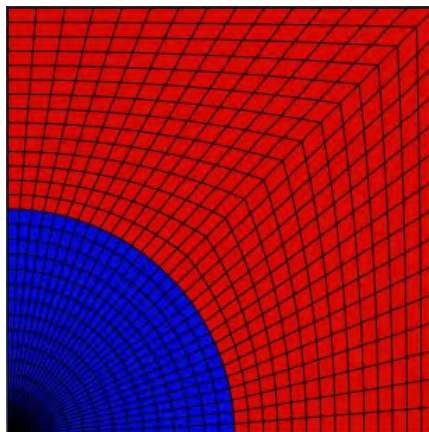

Figure 2.5: Final mesh of a 2D unit cell corresponding to volume fraction $c = 0.10$.

Finally, Fig. 2.6 shows schematically the successive geometric approximations, that lead from the actual three-dimensional prismatic unit cells, to the axisymmetric finite element modeling of the two-dimensional unit cell.
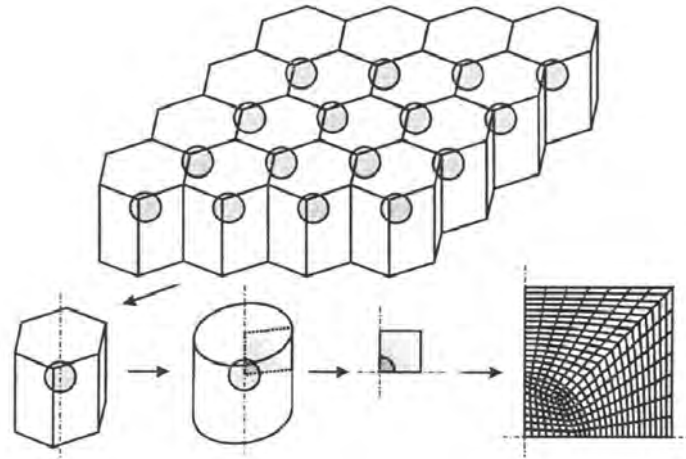
Figure 2.6: Succesive geometric approximations leading to 2D unit cell modeling.

2.3 Deformation and Boundary conditions

Once the mesh has been defined, a "finite strain" analysis is carried out. In order to model a uniaxial tension test, we impose a uniform and vertical displacement on the top side of the mesh until a final elongation of 20% is reached. This can be done by tying all the nodes of the top side to an external node. Then we impose the desired displacement on this node, and we export the reaction force. Along the other three sides of the model, we impose specific boundary conditions, in order to respect the symmetry and periodicity of the infinite series of stacked cells in uniaxial tension.

- All nodes along the midplane ($z = 0$), are constrained to have zero displacement on the z-direction.

- All nodes along the pole (z-axis), are constrained to have zero displacement on the r-direction.

- All nodes on the outer edge of the cell are constrained to have equal displacements along the r-direction.

A schematic representation of the boundary conditions is shown in Figure 2.7.

2.4 Material definition

The two phases involved in our analysis (Austenite and Martensite) are modeled as elastic-plastic materials with $E = 220000 \, MPa$ (Young's modulus) and $\nu = 0.3$ (Poisson's ratio). The hardening behavior of the two phases is described by the following equations:

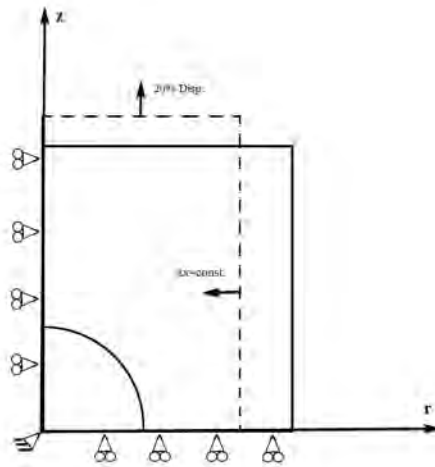**Austenite:** $\quad \sigma_y \left(\bar{\varepsilon}^{p(a)} \right) = 300 + 500 \left(\bar{\varepsilon}^{p(a)} \right)^{0.25},$

Figure 2.7: Schematic depiction of the problem along with the boundary conditions.

Martensite: $\sigma_y\left(\bar{\varepsilon}^{p(m)}\right) = 1200 + 1025\left(\bar{\varepsilon}^{p(m)}\right)^{0.13}$.

The variation of $\sigma_y^{(a)}$ and $\sigma_y^{(m)}$ with $\bar{\varepsilon}^{p(a)}$ and $\bar{\varepsilon}^{p(m)}$ respectively is shown in Fig. 2.8.
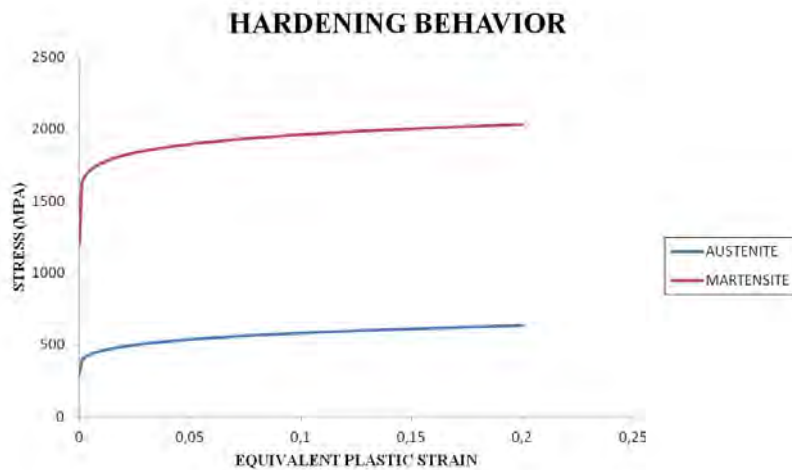

Figure 2.8: Hardening behavior models of austenite and martensite.

In order to simulate the above hardening behavior of the two phases for our analysis, ABAQUS provides a general interface so that the hardening behavior of a particular material can be introduced as a "user subroutine" (UHARD). This subroutine is called at all material calculation points of elements for which the material definition includes user-defined isotropic hardening or cyclic hardening for metal plasticity, and can be used to define a material's isotropic yield behavior.

Such a user subroutine is created, for the special case that one has to model the hardening behavior for more than one material in one analysis (see Appendix A). To create such a user subroutine, one must go through some strict rules regarding all the parameters of the analysis. (For more details on the development of such a user subroutine, see ABAQUS Version 6.12 Documentation [1]).

2.5 Analysis in five different volume fractions

As already mentioned, we would like to get finite element results over a variation of volume fractions for the inclusion particles. This means working with five different models, corresponding to five different volume fractions. Specifically, we will work with the following volume fractions: $c^{(2)} = 0.10, 0.20, 0.30, 0.40, 0.50$. Figure 2.9 shows the deformed finite element meshes, for four different volume fractions, at a final elongation of 20%.
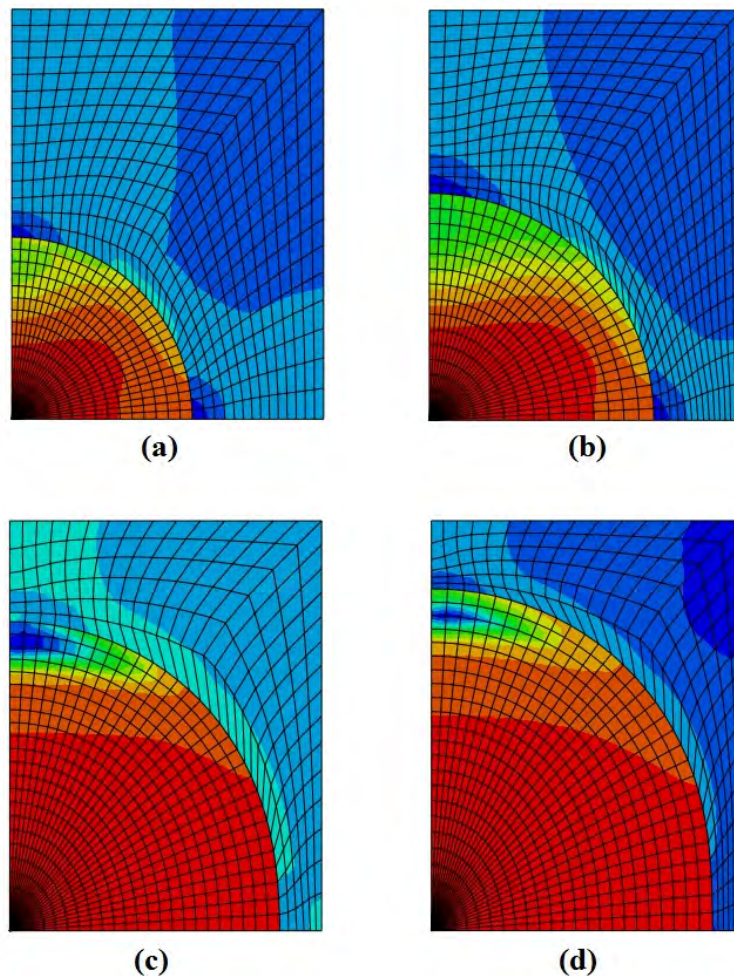

Figure 2.9: Deformed meshes at a final elongation of 20%, for four different volume fractions: (a) $c = 0.10$, (b) $c = 0.20$, (c) $c = 0.40$, (d) $c = 0.50$.

Figures 2.10, 2.11, 2.12, 2.13, and 2.14 show the comparison between the results from the 2D unit cell analysis and the results obtained by the UMAT subroutine, which has been analyzed in previous chapters, for the aforementioned volume fractions. The results are printed on "$\sigma - \varepsilon$" graphs, where σ is the true stress as calculated on the top side of the unit cell and ε is the logarithmic strain, defined as:

$$\varepsilon_{true} = \ln\left(1 + \varepsilon_{nom}\right) = \ln\left(1 + \frac{l - L}{L}\right), \tag{2.2}$$

where L and l are respectively the initial and final lengths of the unit cell in the direction of tension.

Figure 2.10: Comparison of the 2D unit cell analysis with the homogenization theory for $c = 0.10$.

Figure 2.11: Comparison of the 2D unit cell analysis with the homogenization theory for $c = 0.20$.

One can easily see that while we have a good convergence of results, for small volume fractions of the inclusion phase ($c = 10 - 20\%$), as the volume fraction increases, the results obtained from the 2D unit cell analysis, deviate significantly from those obtained through
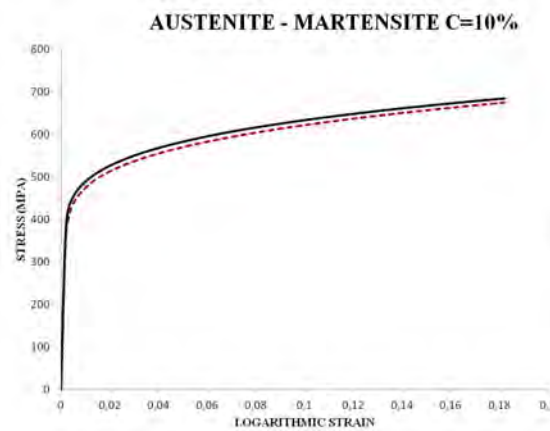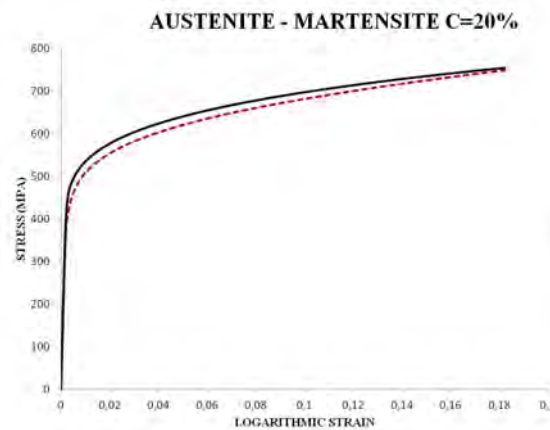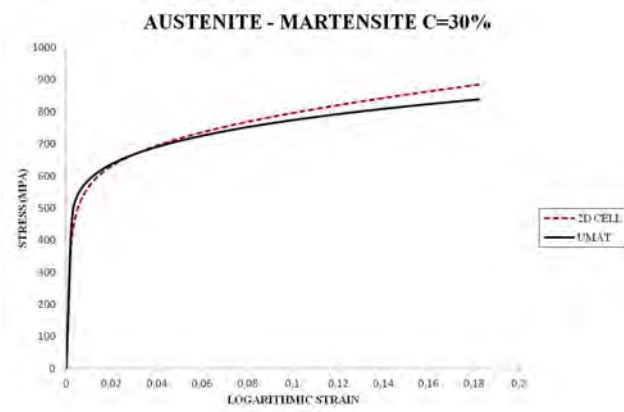
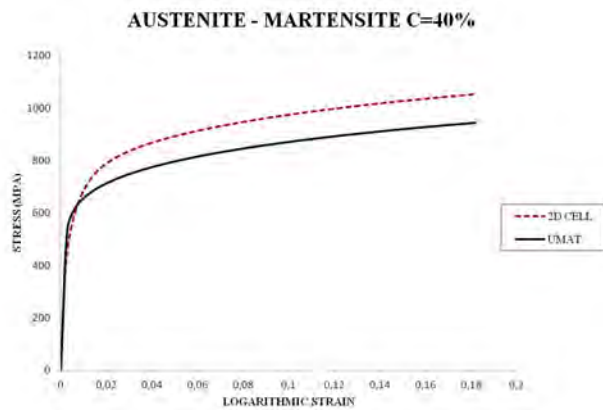Figure 2.12: Comparison of the 2D unit cell analysis with the homogenization theory for $c = 0.30$.

Figure 2.13: Comparison of the 2D unit cell analysis with the homogenization theory for $c = 0.40$.
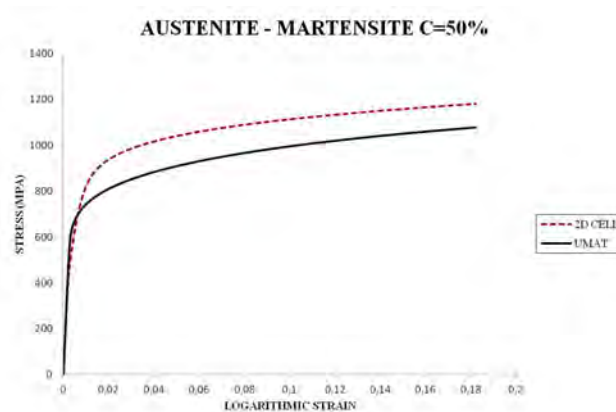
Figure 2.14: Comparison of the 2D unit cell analysis with the homogenization theory for $c = 0.50$.

the UMAT subroutine, thus the homogenization theory. In order to "explain" this deviation, in the next chapter, we will introduce a more realistic 3D unit cell, and we will see that it converges perfectly with the homogenization theory for all the different volume fractions. By that, we conclude that the 2D unit cell can be considered a reliable comparison model, only for the case where the inclusion volume fraction is small. Note again, that the above calculations included two completely different phases, as far as their yields are concerned. That means that the above results should converge even better for a more realistic model, containing phases that are more similar to one another.

Chapter 3

Cubic unit cell

3.1   Introduction

We would like now to compare the theoretical results as were discussed in chapter 1 with an even more realistic finite element simulation than the axisymmetric 2D unit cell that we have already seen in the previous chapter. In this section we work out a 3D unit cell model. In order to simulate more accurately the geometry of a composite material, we consider an infinite periodic media made up of the repetition of cubic unit cells of unit volume $L \times L \times L = 1$. Each 3D unit cell consists of a cubic matrix containing a random distribution of a large number of not overlapping particles, for particle volume fractions up to 50%. Because of the distribution being random as it is, we can consider the overall model as an isotropic one (so that all directions in the unit cell are equivalent).

In order to examine even better the effect of the size dispersion of the filler particles, we examine distributions with particles of the same (monodisperse) and of different (polydisperse) size. In the following sections we will see how we can create such a complex geometry, as well as use it to carry out finite element calculations. Evidently, the accuracy of the solution and the computer time to solve the problem increases with the number of particles in the unit cell, as well as with the complexity of the mesh. According to the parametric studies of Segurado and LIorca [14] a value of $N = 30$ is a sufficiently large number of particles in the unit cell, to approximate overall isotropy.

The first step is to create the geometry of such a unit cell for both monodisperse and polydisperse microstructure, which is then filled out with finite elements in order to carry out our finite element calculations. It is important to mention that for the desired number of particles in the unit cell ($N = 30$), we can create a monodisperse microstructure for up to 30% particle volume fraction.

3.2   Monodisperse microstructure

The monodisperse microstructures are created using a random sequential adsorption algorithm (RSA) (Torquato [16]). The computational software program Mathematica® is used

to generate the coordinates of the particle centers and to define the appropriate periodicity conditions. The particle center positions are generated randomly and sequentially. The particle radius R_m is obtained from the particle volume fraction in the unit cell, as seen below.

$$R_m = L \left(\frac{3\,c}{4\,\pi\,N} \right)^{1/3},$$

(3.1)

where N has been introduced to denote the number of particles in the unit cell and c is the volume fraction of the inclusion material.

Each random particle i is accepted if its center coordinates $\mathbf{X}^i$ verify the following conditions, so that the distance between the particles with other particles and with the boundaries of the cubic cell take a minimum value, that guaranties adequate spatial discretization.

- The center-to-center distance between a new particle i in the sequential algorithm and any previously accepted particle $j = 1, 2, ..., i-1$ has to exceed the minimum value $s_1 = 2\,R_m\,(1 + d_1)$, where the offset distance d_1 is fixed here at $d_1 = 0.02$. If the surface of particle i cuts any of the cubic unit cell surfaces, this condition has to be checked with the particle near the opposite surface because the microstructure of the composite is periodic. This condition can be compactly written in the form:

$$\left\| \mathbf{X}^i - \mathbf{X}^j - \mathbf{h} \right\| \geq s_1,$$

(3.2)

  where $\mathbf{X}^i$, $\mathbf{X}^j$ denote the location of the center of particles i, j and $\mathbf{h}$ is a vector with entries for each of its three Cartesian components with respect to the principal axes of the cubic unit cell.

- Particle surface should be sufficiently distant from the boundaries of the unit cell to prevent the presence of distorted finite elements during meshing. This is enforced by the inequalities:

$$\left| X_k^i - R_m \right| \geq s_2 \qquad \text{and} \qquad \left| X_k^i + R_m - L \right| \geq s_2, \qquad k = 1, 2, 3,$$

(3.3)

  where $s_2 = d_2\,R_m$ with d_2 being fixed here at $d_2 = 0.05$.

Figure 3.1 shows representative unit cells of the monodisperse case, generated by the above-described algorithm for $N = 30$, with three different particle volume fractions.

We can create a monodisperse microstructure for up to 30% particle volume fraction.

3.3   Polydisperse microstructure

We consider now polydisperse microstructures, which can be used for volume fractions up to 50%. Polydisperse microstructures are constructed by means of a similar constrained adsorption algorithm. The main difference here is that we use three different families of particle sizes. This can help us create more complex geometries, and achieve particle volume
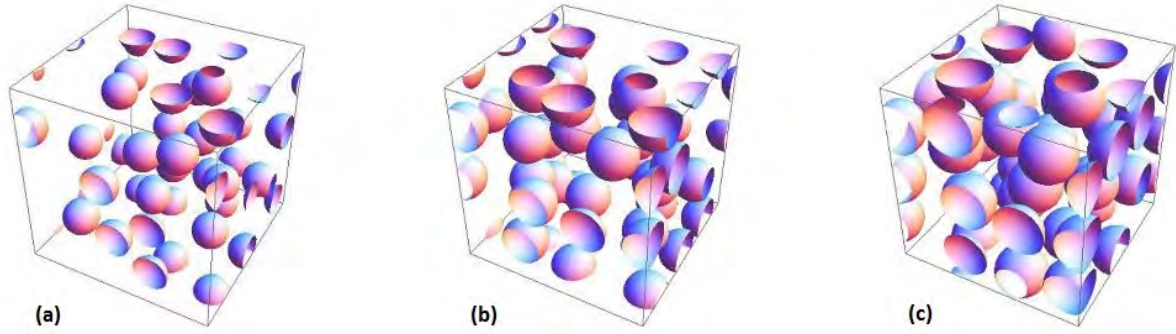
Figure 3.1: Representative unit cells containing $N = 30$ randomly distributed spherical particles of monodisperse sizes with three different concentrations: (a) $c = 0.10$, (b) $c = 0.20$, (c) $c = 0.30$.

fractions up to 50%. As one can easily notice, there can be many combinations of these three different particle sizes. In order to narrow down the distribution possibilities, we consider the following procedure.

- Three different families of particles with radii $R_p^{(I)}$ and concentrations $c^{(I)}$ ($I = 1, 2, 3$) are utilized, such that:

$$\left\{ R_p^{(1)}, R_p^{(2)}, R_p^{(3)} \right\} = \left\{ R_p, \frac{7}{9}\, R_p, \frac{4}{9}\, R_p \right\} \tag{3.4}$$

and

$$\left\{ c^{(1)}, c^{(2)}, c^{(3)} \right\} = \left\{ 0.5\, c, 0.25\, c, 0.25\, c \right\} \tag{3.5}$$

with $R_p = L \left(\frac{3\, c^{(1)}}{4\, \pi\, N_p} \right)^{1/3}$ and $c^{(1)} + c^{(2)} + c^{(3)} = c$, where N_p stands for the number of particles with the largest radius $R_p^{(1)} = R_p$ in the unit cell and c the total volume fraction.

- The microstructures are generated sequentially by first adding particles with the largest radius $R_p^{(1)}$ until the concentration reaches the value $c^{(1)} = 0.5\, c$, subsequently adding particles with radius $R_p^{(2)}$ until $c^{(1)} + c^{(2)} \simeq 0.75\, c$, and finally adding particles with the smallest radius $R_p^{(3)}$ until $c^{(1)} + c^{(2)} + c^{(3)} \simeq c$.

In following this construction process, we note that a target concentration c can only be achieved approximately (up to a small error that depends on the various choices of the parameters). Similarly to conditions (3.2), (3.3) and (3.3), in order to guarantee adequate spatial discretization, the randomly generated coordinates of the centers of the particles are enforced to satisfy the following constraints. That means that again, particle i is accepted, if center coordinates $\mathbf{X}^i$ verify the following conditions:

- The center-to-center distance between a new particle i in the sequential algorithm and any previously accepted particle $j = 1, 2, ..., i-1$ has to exceed the minimum value s_1. This condition can be expressed also as:

$$\left\| \mathbf{X}^i - \mathbf{X}^j - \mathbf{h} \right\| \geq s_1, \tag{3.6}$$

where $s_1 = \left(R_p^{(m_i)} + R_p^{(m_j)} \right) (1 + d_1)$.

- The particles should be sufficiently distant from the boundaries of the unit cell as enforced by the inequalities:

$$\left| X_k^i - R_p^{(m_i)} \right| \geq s_2 \qquad \text{and} \qquad \left| X_k^i + R_p^{(m_i)} - 1 \right| \geq s_2, \qquad k = 1, 2, 3, \tag{3.7}$$

where $s_2 = d_2 R_p^{(m_i)}$. For $i, j = 1, 2, ..., N$, N again denoting the total number of particles in the unit cell. Here, the offset parameters are set at $d_1 = 0.02$ and $d_2 = 0.05$ as in the monodisperse case, and the superscript $m_i = 1, 2, 3$ has been introduced to denote the size of the sphere that should be added at step i in the sequential construction process, namely, $m_i = 1$ if $c^{(m_i)} \leq c^{(1)}$, $m_i = 2$ if $c^{(1)} < c^{(m_i)} \leq c^{(1)} + c^{(2)}$, and $m_i = 3$ if $c^{(1)} + c^{(2)} < c^{(m_i)}$.

Guided by a similar parametric study of the monodisperse microstructures, we utilize $N_p = 10$ (10 spheres of the largest radius), which results to unit cells containing a total of $N = 36$ particles. As discussed in section 3.1, such unit cells are sufficiently large to be representative of isotropic microstructures. Figure 3.2 displays sample unit cells generated by the above-described algorithm for $N = 36$ with three different particle volume fractions.
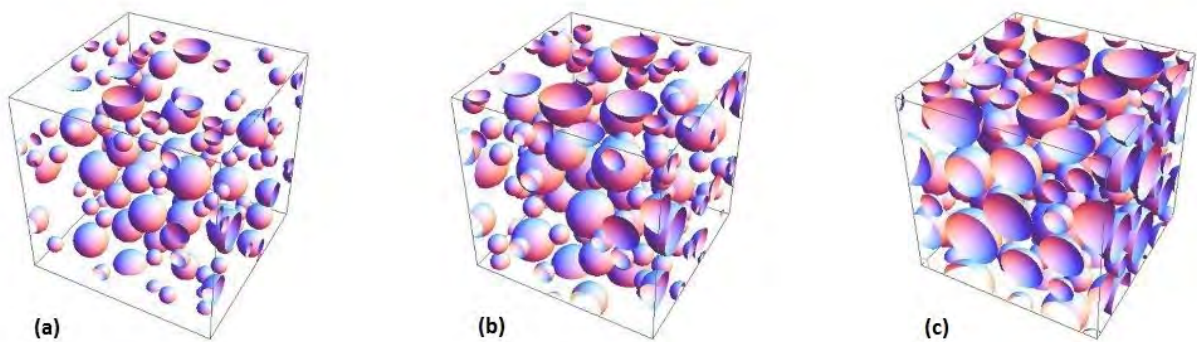

Figure 3.2: Representative unit cells containing $N = 36$ randomly distributed spherical particles of three different sizes with three different concentrations: (a) $c = 0.10$, (b) $c = 0.20$,(c) $c = 0.40$.

It is important to mention that the various parameters of the RSA can be modified in order to produce various combinations of particle positions, resulting to a different geometry

each time. However, due to the randomness of the dispersion, the unit cells remain isotropic. The above allegation will be proved later, by testing different geometries for a specific volume fraction.

3.4 Meshing

Having constructed the monodisperse and polydisperse microstructures of interest, we now turn to their discretization. The first step would be to create a finite element mesh for them. For that, we make use of the mesh generator code Netgen (Schoberl [13]), which has the capability to create periodic meshes, as required here. Ten-node tetrahedral hybrid (2nd order) elements are utilized in order to handle exactly (in a numerical sense) the elastoplastic behavior of our materials of interest. Since the computations are carried out using the ABAQUS general purpose finite element code, we make use in particular of the C3D10H hybrid elements available in this code (see ABAQUS Version 6.12 Documentation [1]).

Another important issue we have to consider is the complexity of the mesh. We have already mentioned that the accuracy of the calculations increases with the complexity of the mesh, but so does the computer time required to solve the problem. Sometimes a very fine mesh could make the calculations impossible to complete using the existing computers. On the contrary, using a coarse mesh doesn't give as accurate results. Taking into account existing studies and testing various meshes of our own, we conclude that the use of a fine mesh (100,000 to 240,000 elements) gives us both accurate results and a reasonable computer time (24h-48h).
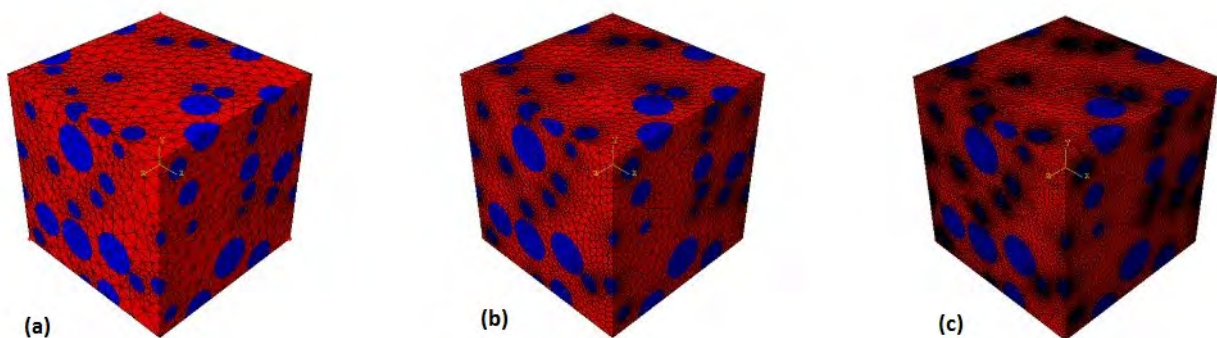

Figure 3.3: Three Representative meshes of increasing refinement for a distribution of polydisperse particles, with volume fraction $c = 0.20$. Where (a) stands for a coarse mesh of 39,563 elements, (b) is a fine mesh of 255,866 elements and (c) is a very fine mesh consisted of 1,425,549 elements.

The number of elements in a fine mesh varies also with the volume fraction of the unit

cell. Figure 3.3 shows three meshes of increasing refinement for a volume fraction of $c = 0.20$ and the the corresponding number of elements for each case.

3.5 Boundary conditions and materials

Periodic boundary conditions have to be applied on the unit cell faces. These periodic boundary conditions can be mathematically expressed as follows:

$$
\begin{aligned}
u_k\left(L, X_2, X_3\right) - u_k\left(0, X_2, X_3\right) &= \left(\bar{F}_{k1} - \delta_{k1}\right) L, \\
u_k\left(X_1, L, X_3\right) - u_k\left(X_1, 0, X_3\right) &= \left(\bar{F}_{k2} - \delta_{k2}\right) L, \\
u_k\left(X_1, X_2, L\right) - u_k\left(X_1, X_2, 0\right) &= \left(\bar{F}_{k3} - \delta_{k3}\right) L,
\end{aligned}
\tag{3.8}
$$

where the components u_k and X_k with $(k = 1, 2, 3)$ refer to a Cartesian frame of reference with origin placed at the corner of the cubic unit cell whose axes $\mathbf{e}_k$ are aligned with the principal axes of the cubic unit cell, δ_{kl} denotes the Kronecker delta, and $\bar{\mathbf{F}}$ is the average (macroscopic) deformation gradient. The above periodic boundary conditions are created using the mesh generator code Netgen and printed within a (.mpc) file, and then are imported in ABAQUS using the "*EQUATION" command.

The material definition is done as in chapter 2.4. Again we use the same UHARD subroutine, as we did for the 2D unit cell (see Appendix A), which simulates the properties of austenite for the matrix phase and martensite for the spherical inclusions. For more information on the material definitions see section 2.4.

3.6 Loading

In order to perform a uniaxial tension test, we apply incrementally a uniform displacemnet on the top face of the unit cell until a final elongation of 15% is achieved. Figure 3.4 shows the deformed monodisperse meshes for volume fractions ($c \simeq 0.10, c \simeq 0.20, c \simeq 0.30$) and Fig. 3.5 shows the deformed meshes for the polydisperse case and for volume fractions ($c \simeq 0.10, c \simeq 0.20, c \simeq 0.30, c \simeq 0.40$).

Once we have set the entire uniaxial tension test, two important issues have to be considered. One is whether a random cubic cell is actually isotropic. To check that, we impose the same deformation first on the top face, then on the right and finally on the front, across the three axis (shown in Fig. 3.6), and we see that each time, the results are the same.

The other issue is making sure that the sphere distribution, for a specific volume fraction, given that the distribution is random, does not affect the final results. That means that any different sphere distribution should result in the same results being exported. To ensure that, we carry out the same analysis for different meshes of the four volume fractions that are examined here. The results are shown in the following graphs (Figures: 3.7, 3.8, 3.9, 3.10). One can see that even though we have a relatively big difference between the number of elements and the degrees of freedom for each mesh, the results of each case have a deviation
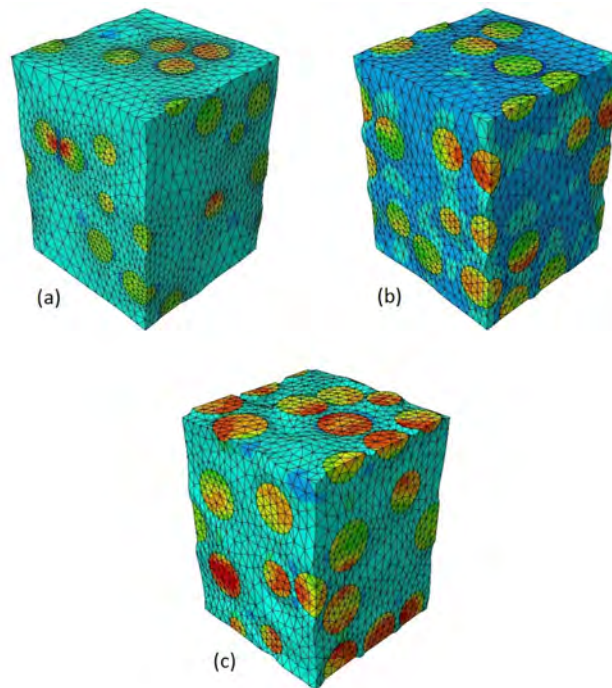
Figure 3.4: Deformed meshes of the monodisperse case, for a final elongation of 15%, where: (a) is for $c = 0.10$, (b) is for $c = 0.20$ and (c) is for $c = 0.30$.
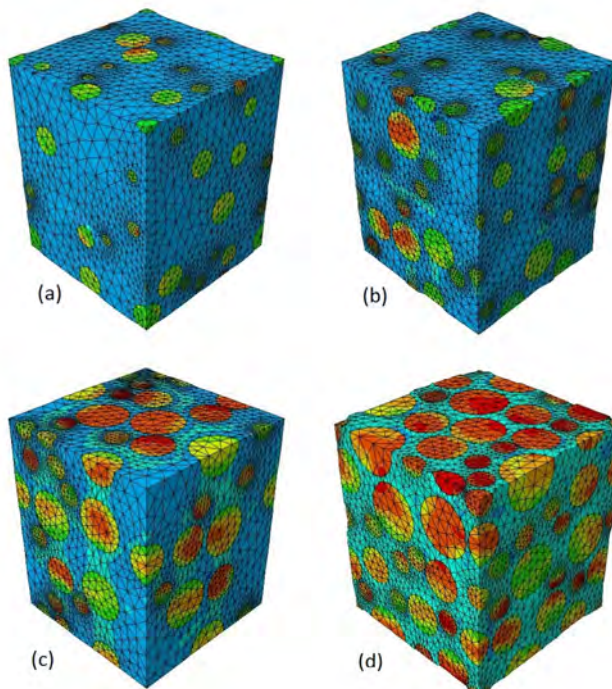

Figure 3.5: Deformed meshes of the polydisperse case, for a final elongation of 15%, where: (a) is for $c = 0.10$, (b) is for $c = 0.20$, (c) is for $c = 0.30$ and (d) is for $c = 0.40$.
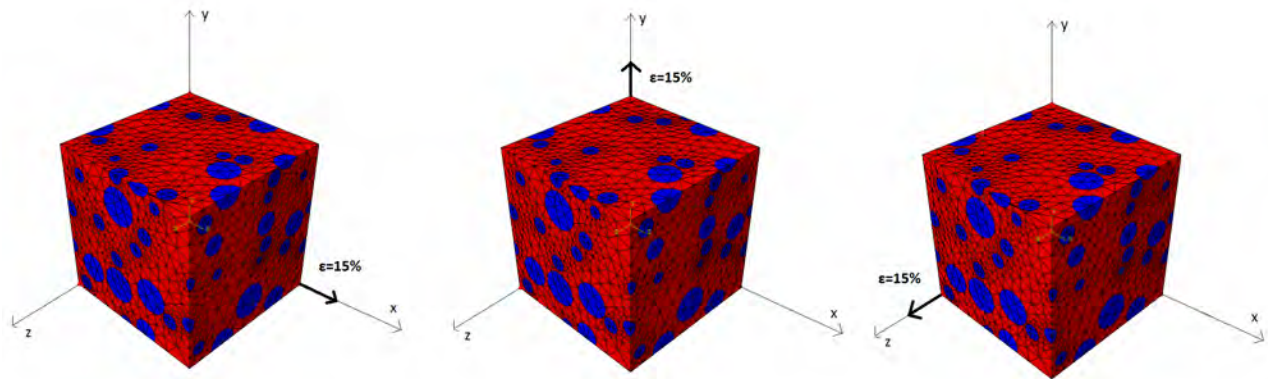
Figure 3.6: Loading of the three different faces of a polydisperse unit cell for $c = 0.20$.

that is always smaller than 1%. Hence, we can concur that each cubic unit cell can be considered as a random and isotropic one.
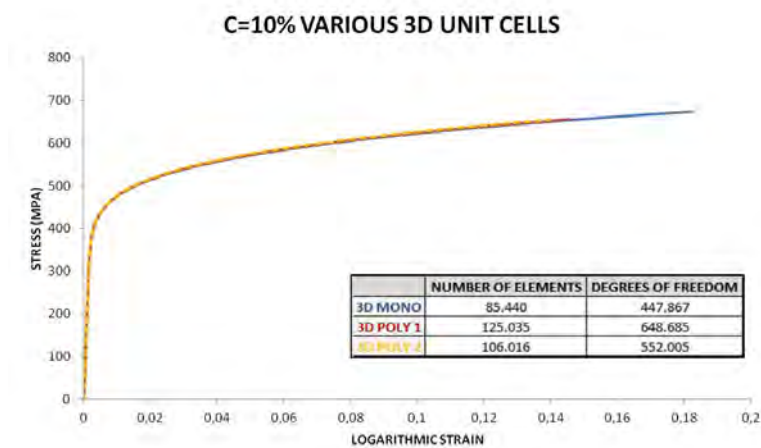

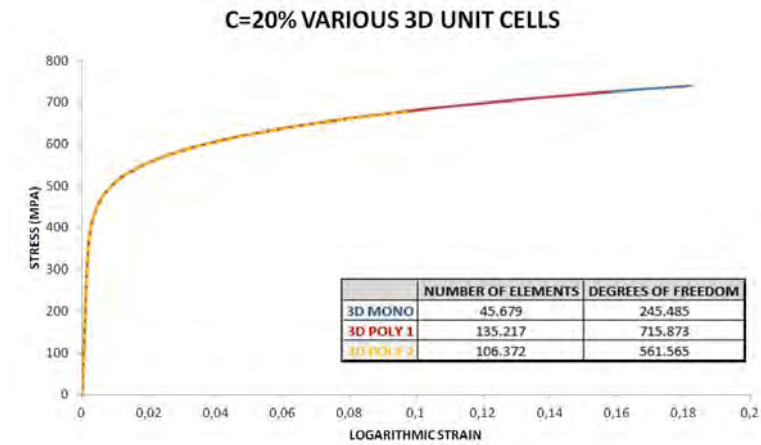Figure 3.7: Comparison of three different meshes for a cubic unit cell with $c = 0.10$.

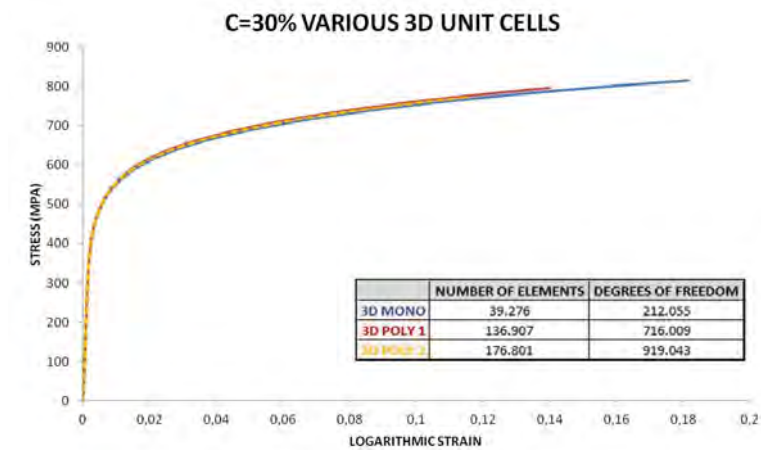Figure 3.8: Comparison of three different meshes for a cubic unit cell with $c = 0.20$.

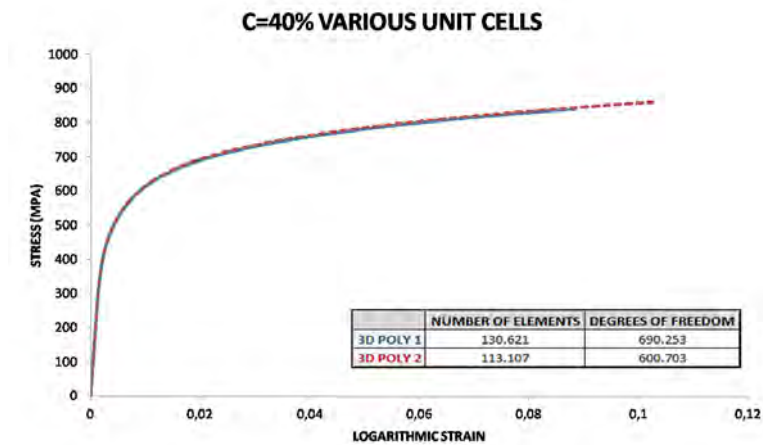Figure 3.9: Comparison of three different meshes for a cubic unit cell with $c = 0.30$.

Figure 3.10: Comparison of two different meshes for a cubic unit cell with $c = 0.40$.

Chapter 4

Comparison for a two-phase simple case

In this section we would like to compare the results of the cubic unit cell calculations with those of the homogenization theory presented in the previous sections. The homogenization theory is put to the test through the UMAT subroutine as we have explained. In Figs. 4.1, 4.2, 4.3, 4.4, and 4.5 we present these results together with the results of the 2D axisymmetric unit cell.

One can easily notice that, for small volume fractions, all unit cells give equally good results with the homogenization theory. However, as the volume fractions increases, it is obvious that the 2D unit cell can not be considered realistic as its results deviate from those of the homogenization theory and the 3D unit cell. One important observation is that the results of the cubic unit cell agree well with the results of the homogenization theory no matter the volume fraction.
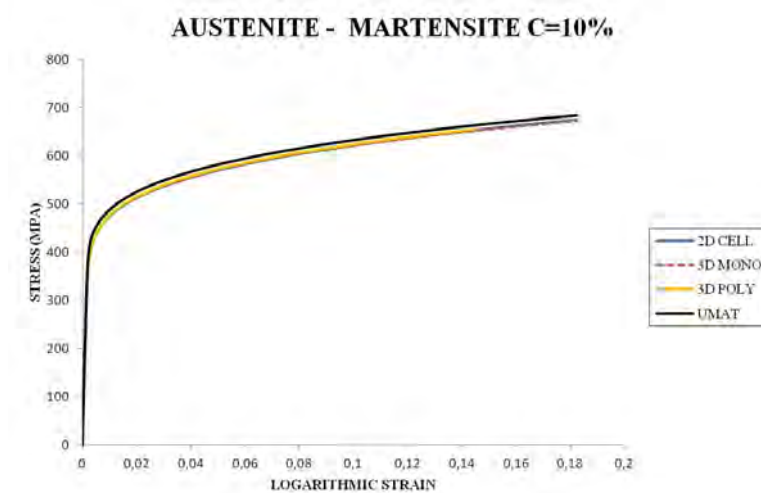

Figure 4.1: Comparison of various unit cells with the homogenization theory for $c = 0.10$.
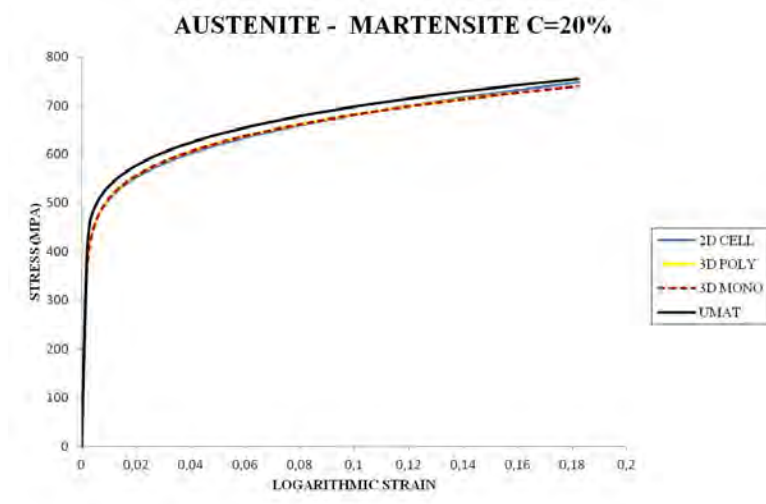
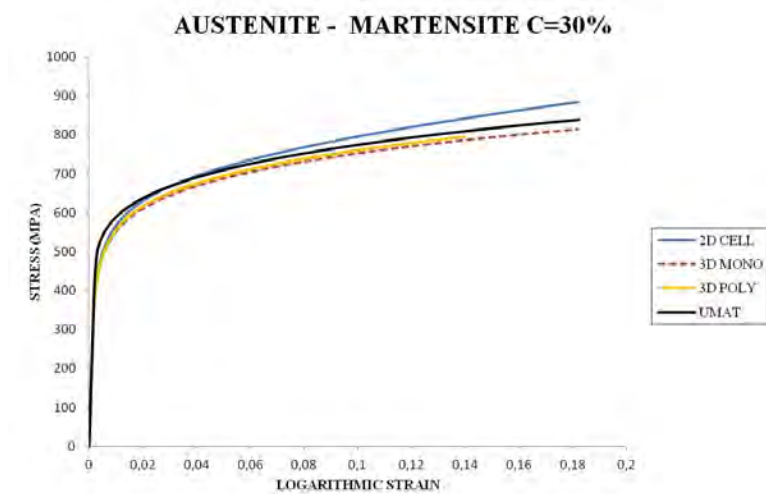Figure 4.2: Comparison of various unit cells with the homogenization theory for $c = 0.20$.

Figure 4.3: Comparison of various unit cells with the homogenization theory for $c = 0.30$.
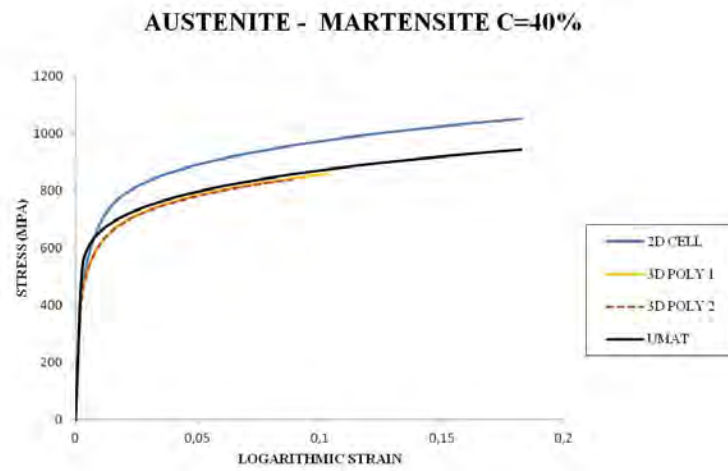
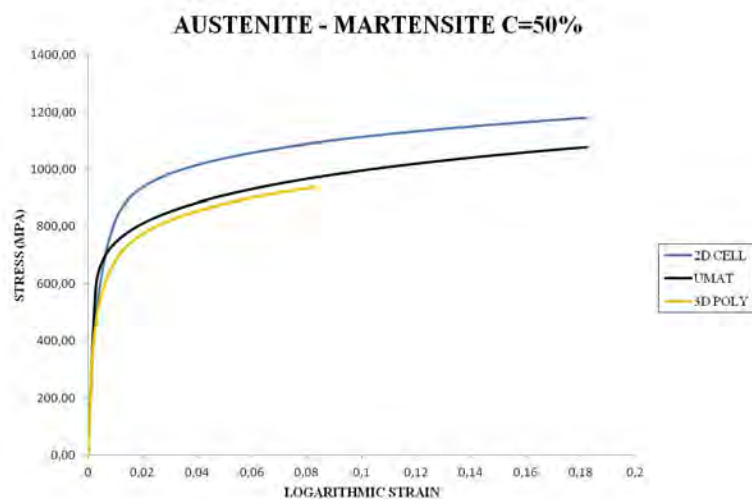Figure 4.4: Comparison of various unit cells with the homogenization theory for $c = 0.40$.

Figure 4.5: Comparison of various unit cells with the homogenization theory for $c = 0.50$.

Chapter 5

Three-phase cubic unit cell

5.1 Introduction

Similarly to the procedure described above, we can create a three-phase cubic unit cell, consisted of a cubic matrix, containing spherical inclusions of two different phases. Specifically, using a Random Sequential Algorithm similar to the one described in section 3.3, we can create two different three-phase unit cells, called from now on $V1$ and $V2$.

5.2 Constructing the microstructure

Again, as for the two-phase polydisperse microstructure, we use a group of spheres with different radii, one for each of the inclusion phases. Let c_0 denote the volume fraction of the matrix phase 0, and c_1, c_2 the volume fractions of the inclusion phases 1 and 2 respectively. That makes a total $c_{tot} = c_1 + c_2$ of inclusion phases, with $c_0 + c_{tot} = 1$. The whole procedure can be summarized in the following steps.

- We make use of three different families of particles with radii $R_p^{(I)}$ ($I = 1, 2, 3$) and concentrations $c^{(I)}$ for each of the inclusion phases. For our case, we use:

$$\left\{ R_{px}^{(1)}, R_{px}^{(2)}, R_{px}^{(3)} \right\} = \{1, 0.5, 0.1\} \tag{5.1}$$

  and

$$\left\{ c_x^{(1)}, c_x^{(2)}, c_x^{(3)} \right\} = \{0.6\, c_x, 0.2\, c_x, 0.2\, c_x\} \tag{5.2}$$

  with $x = 1, 2$ denoting each of the two different inclusion phases.

- We add: $(c_1/c_{tot}) \times c_1^{(1)} \times c_{tot}$ of particles with radius $R_{p1}^{(1)}$ of phase 1, and particles with radius $R_{p2}^{(1)}$ of phase 2 until the rest of $c_1^{(1)} \times c_{tot}$ is filled. Then we do the same for the second group of spheres. We add $(c_1/c_{tot}) \times c_1^{(2)} \times c_{tot}$ of particles with radius $R_{p1}^{(2)}$ of phase 1 and particles with radius $R_{p2}^{(2)}$ of phase 2, until the rest of $c_1^{(2)} \times c_{tot}$ is filled. The same goes for sphere group 3.

  The only difference between $V1$ and $V2$ is that for the $V2$ unit cell we use more groups of spheres of the same radii to construct the microstructure. That makes the $V2$ microstructure

a more complex but also more random and realistic model of a three-phase steel.

In order to guarantee adequate spatial discretization, again the randomly generated coordinates of the centers of the particles are enforced to satisfy constraints similar to (3.6) and (3.7). Figure 5.1 shows representative $V1$ and $V2$ unit cells for volume fractions $c_0 = 60\%$, $c_1 = 25\%$ and $c_2 = 15\%$.
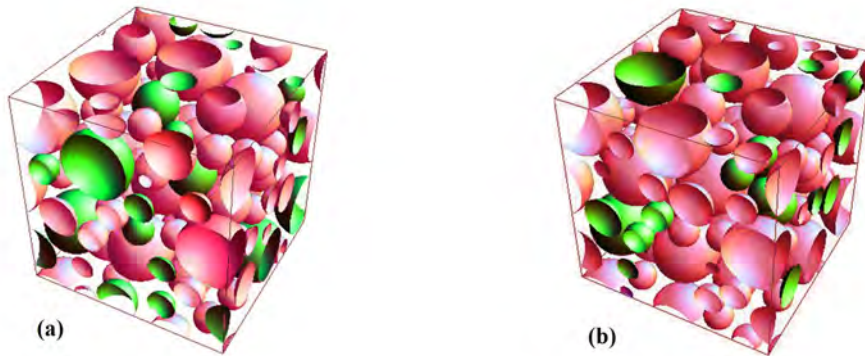

Figure 5.1: Three-phase unit cells containing $c_1 = 25\%$ and $c_2 = 15\%$ of inclusion phases, where (a) is for $V1$ and (b) is for $V2$.

5.3 Meshing and Material Definition

The meshing of the microstructure is done similarly to that of section 3.4 and the two-phase polydisperse unit cell. Again, ten-node tetrahedral hybrid (2nd order) elements are utilized (C3D10 in ABAQUS). We also make use of a "fine" meshing with the help of the NetGen mesh generator code, resulting to a mesh of 120,000 to 130,000 elements for both $V1$ and $V2$ unit cells. Figure 5.2 shows two typical such meshes for $V1$ and $V2$ unit cells. The same goes for the boundary contitions witch are exactly the same as those used in chapter 3.5.

The material properties are imported through a UHARD subroutine (User HARdening), similarly to the previous chapters. The only difference here is that one has to "call" the UHARD subroutine during the process for three different phases. For our examples, we assume a ferritic matrix phase, containing 25% bainite and 15% martensite. The hardening behavior of the three phases is described by the following equations:

Ferrite: $\sigma_y \left(\bar{\varepsilon}^{p(m)} \right) = 290 + 690 \left(\bar{\varepsilon}^{p(m)} \right)^{0.47}$

Bainite: $\sigma_y \left(\bar{\varepsilon}^{p(m)} \right) = 810 + 753 \left(\bar{\varepsilon}^{p(m)} \right)^{0.25}$
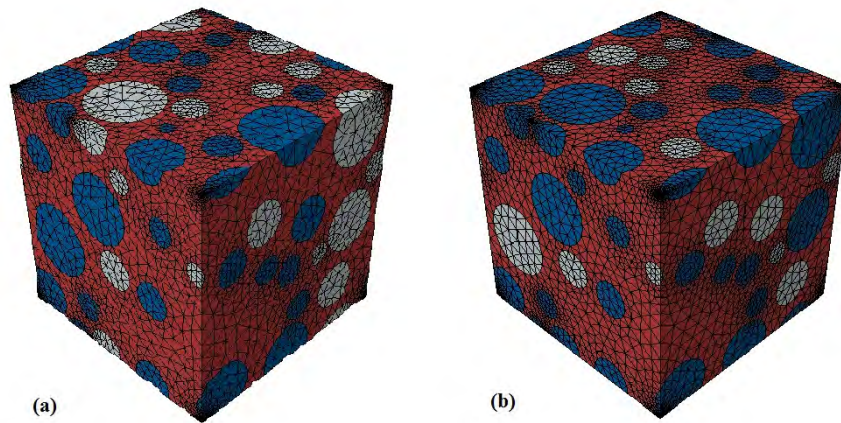
Figure 5.2: Three-phase unit cell meshes, where (a) is for $V1$ and (b) is for $V2$.

Martensite: $\quad \sigma_y \left(\bar{\varepsilon}^{p(m)} \right) = 1200 + 1025 \left(\bar{\varepsilon}^{p(m)} \right)^{0.13}$

The hardening curves for the above models, that are used to describe the actual behavior of ferrite, bainite and martensite are depicted in Fig. 5.3.
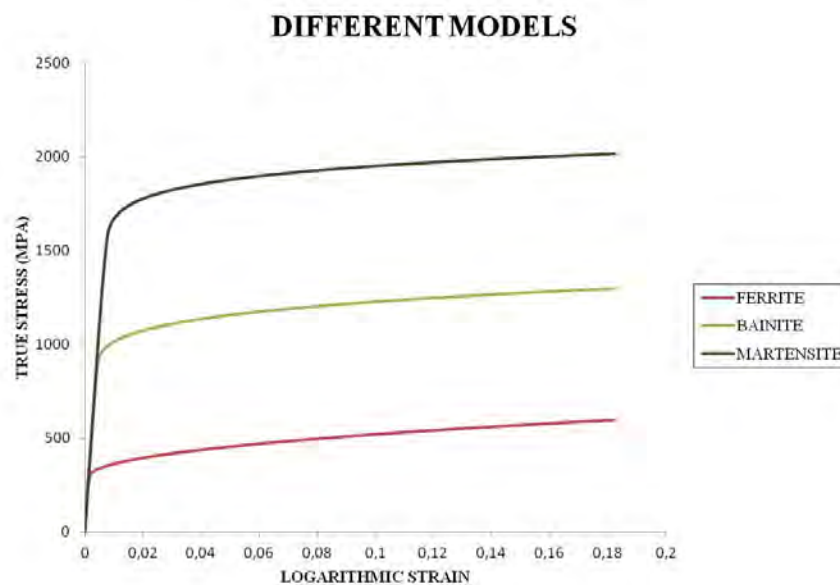

Figure 5.3: Hardening behavior models of ferrite, bainite and martensite.

5.4 Loading

An important issue that we have to take into consideration is the isotropy of the three-phase unit cells. We would like the above unit cells to produce the same results regardless of the direction of the loading. To ensure that, we perform a simple uniaxial tension test along the

three different axis, this is depicted in Fig. 5.4. As we see in Fig. 5.5 the results in each case are exactly the same. That means the above unit cells are indeed isotropic.
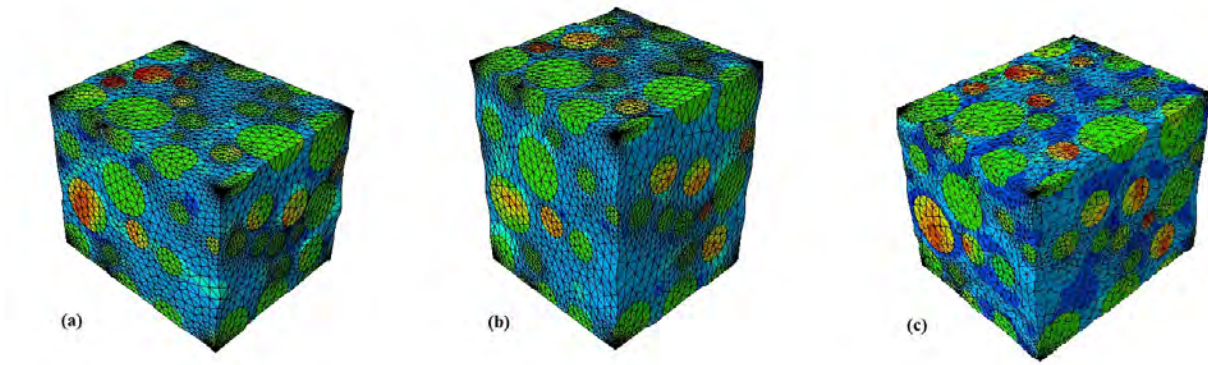

Figure 5.4: Loading on three different directions for a $V2$ three-phase unit cell.
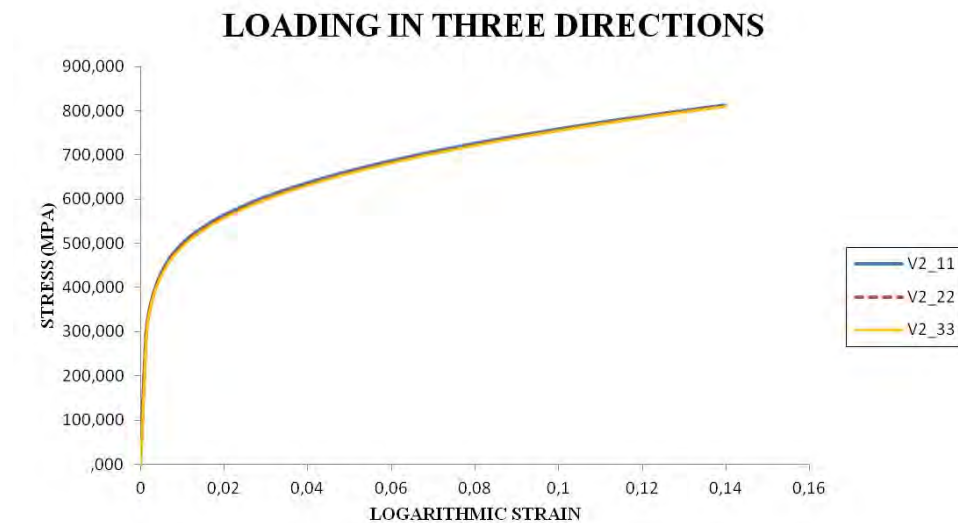
Figure 5.5: Comparison between loadings on different directions.

Once we have ensured the isotropy and functionality of the unit cells, we perform a uniaxial tension test on both $V1$ and $V2$ for $c_{FERR} = 60\%$, $c_{BAIN} = 25\%$ and $c_{MART} = 15\%$. The results are then compared to that of a single element test, using the UMAT subroutine for 3 different phases and volume fractions as above. We can see in Fig. 5.6 that even though we use three phases with completely different yield stresses, we achieve a satisfactory agreement between the unit cells and the homogenization theory.

Figure 5.6: Comparison between $V1$, $V2$ and the homogenization theory.

Chapter 6

Conclusion

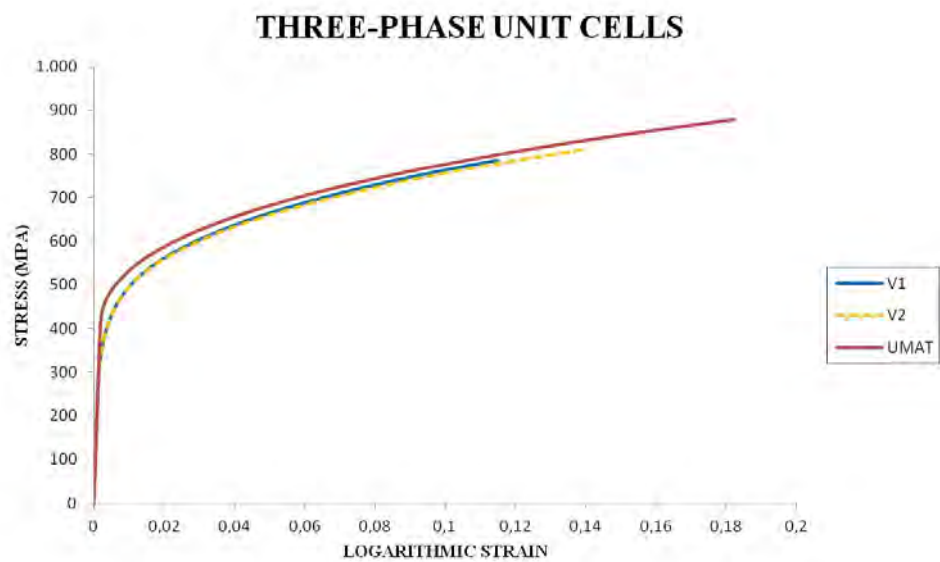In this thesis we dealt with the problem of predicting the overall properties of a composite material. Specifically we worked on multiphase steels, which are widely used by the automotive industry and not only.

Firstly, a homogenization theory is presented, that is used to predict the mechanical properties of a composite, given those of its constituent phases. Then, this technique was implemented into ABAQUS finite element program through a UMAT (User MATerial) subroutine.

A series of 2D and 3D unit cells were created for the simulation of the microstructure in a multiphase steel and finite element calculations were carried out.

The main focus of this thesis was on the creation of 3D cubic unit cells, which offer a great potential when it comes to modeling complex microstructures. Throughout our calculations, we can see that the results of the homogenization theory agree well with the predictions of the unit cell calculations over a range of volume fractions of the inclusion phase.

Bibliography

[1] ABAQUS, ©Dassault Systemes, 'Analysis Users Manual, Version 6.12', (2012).

[2] N. Aravas, 'On the numerical integration of a class of pressure-dependent plasticity models', *Int. J. Num. Meth. Engng.* **24** (1987) 1395–1416.

[3] A. Giompliakis, I. Papadioti, K. Danas, N. Aravas, 'Constitutive Modeling of TRIP Steels', *5th Panhellenic Conference on Metallic Materials* (2013).

[4] E. H. Kaufman Jr., D. J. Leeming, G. D. Taylor, 'An ODE-based approach to nonlinearly constrained minimax problems', *Numerical Algorithms* **9** (1995) 25–37.

[5] A. Kumar, S. B. Singh, K. K. Ray, 'Influence of bainite/martensite-content on the tensile properties of low carbon dual-phase steels', *Materials Science and Engrg A* **474** (2008) 270–282.

[6] O. Lopez-Pamies, T. Goudarzi, K. Danas, 'The nonlinear elastic responce of suspensions of rifid inclusions in rubber: II-A simple explicit approximation for finite-concentration suspensions', *J. Mech. A/Solids* **61** (2013) 19–37.

[7] J.C. Michel, H. Moulinec, P. Suquet, 'Effective properties of composite materials with periodic microstructure: A computational approach', *Comput. Meth. Appl. Mech. Engrg.* **172** (1999) 109–143.

[8] I. Papatriantafillou, M. Agoras, N. Aravas, G. Haidemenopoulos, 'Constitutive modeling and finite element methods for TRIP steels', *Comput. Meth. Appl. Mech. Engrg.* **195** (2006) 5094–5114.

[9] I. Papatriantafillou, 'TRIP steels: Constitutive modeling and computational issues', *Ph.D. Thesis, University of Thessaly* (2005).

[10] P. Ponte Castañeda, 'The effective mechanical properties of nonlinear isotropic composites', *J. Mech. Phys. Solids* **39** (1991) 45–71.

[11] P. Ponte Castañeda, 'Nonlinear composite nmaterials: Effective constitutive behavior and microstructure evolution', in *Continuum Micromechanics*, CISM Courses and Lectures, ed. P. Suquet, vol. 377 (1997), pp. 131–195, Springer-Verlag.

[12] P. Ponte Castañeda, 'Nonlinear composites', *Advances in Applied Mechanics* **34** (1998) 171–302.

[13] J. Schoberl, 'Netgen an advancing front 2d/3d-mesh generator based on abstract rules', *Computer Visual Science* (1997) 41–52.

[14] J. Segurado, J. Lliorca, 'A numerical approximation to the elastic properties of sphere-reinforced composites', *J. Mech. A/Solids* **50** (2002) 2107–2121.

[15] P. M. Suquet, 'Bounds and estimates for the overall properties of nonlinear composites', in *Micromechanics of Materials*, edited by J.J. Marigo and G. Rousselier, Eyrolles, Paris, 1993, pp. 361–382.

[16] S. Torquato, *Random Heterogeneous Materials: Microstructure and Macroscopic Properties*, Springer-Verlag, New York, Inc. (2002).

Appendix A

UHARD subroutine

```
      SUBROUTINE UHARD(SYIELD,HARD,EQPLAS,EQPLASRT,TIME,DTIME,TEMP,
     +      DTEMP,NOEL,NPT,LAYER,KSPT,KSTEP,KINC,
     +      CMNAME,NSTATV,STATEV,NUMFIELDV,
     +      PREDEF,DPRED,NUMPROPS,PROPS)
C
      INCLUDE 'ABA_PARAM.INC'
C
      CHARACTER*80 CMNAME
      DIMENSION HARD(3),STATEV(NSTATV),TIME(1),
     +          PREDEf(NUMFIELDV),DPRED(1),PROPS(1)
      DIMENSION YIELD(4),H(4)
      DIMENSION A(4),B(4),AN(4)
C
      EBAR=EQPLAS
C
      A(1)=290.D0
      A(2)=810.D0
      A(3)=300.D0
      A(4)=1200.D0
C
      B(1)=690.D0
      B(2)=753.D0
      B(3)=500.D0
      B(4)=1025.D0
C
      AN(1)=0.47D0
      AN(2)=0.25D0
      AN(3)=0.25D0
      AN(4)=0.13D0
C
```

```
      E0=1.D-3
      DO I=1,4
        IF (EBAR.GE.0.D0.AND.EBAR.LE.E0) THEN
          AA= B(I)*(2.D0-AN(I))*(3.D0-AN(I))/(2.D0*E0**(1.D0-AN(I)))
          BB=-B(I)*(1.D0-AN(I))*(3.D0-AN(I))/E0**(2.D0-AN(I))
          CC= B(I)*(1.D0-AN(I))*(2.D0-AN(I))/(2.D0*E0**(3.D0-AN(I)))
          YIELD(I)=A(I)+AA*EBAR+BB*EBAR**2+CC*EBAR**3
          H(I)=AA+2.D0*BB*EBAR+3.D0*CC*EBAR**2
        ELSE
          YIELD(I)=A(I)+B(I)*EBAR**AN(I)
          H(I)=B(I)*AN(I)/EBAR**(1.D0-AN(I))
        ENDIF
      ENDDO
C
      IF (CMNAME.EQ.'FERRITE') I=1
      IF (CMNAME.EQ.'BAINITE') I=2
      IF (CMNAME.EQ.'AUSTENITE') I=3
      IF (CMNAME.EQ.'MARTENSITE') I=4
      SYIELD=YIELD(I)
      HARD(1)=H(I)
C
      RETURN
      END
C
C*****************************************************************************
C
```